Research Article Vol. 60, No. 27 / 20 September 2021 / Applied Optics 8349

applied optics

Fluorescence hyperspectral imaging system for analysis and visualization of oil sample composition and thickness

Qingsheng Xue,[1,*] Ming Qi,[1] Zhanfeng Li,[2] Bai Yang,[1] Wenhao Li,[2] Fupeng Wang,[1] and Qian Li[1]

[1]College of Information Science and Engineering, Ocean University of China, Qingdao, Shandong 266100, China
[2]Changchun Institute of Optics, Fine Mechanics and Physics, Chinese Academy of Sciences Changchun 130033, China
*Corresponding author: xueqingsheng@ouc.edu.cn

Received 2 June 2021; revised 21 August 2021; accepted 21 August 2021; posted 23 August 2021 (Doc. ID 432851); published 14 September 2021

In this paper, a compact fluorescence hyperspectral imaging system based on a prism-grating-prism (PGP) structure is designed. Its spectrometer spectral range is 400–1000 nm with a spectral resolution of 2.5 nm, and its weight is less than 1.7 kg. The PGP imaging spectrometer combines the technical advantages of prism and grating, by not only using six lenses for imaging and collimation to realize the dual telecentres of object and image but also having a "straight cylinder" structure, which makes the installation and adjustment simple, compact, and stable. By the push-broom method, we obtained the three-dimensional cubic data of different oil products. By normalization processing, minimum noise separation transformation processing, visualization processing, and support vector machine classification processing of different oil fluorescence hyperspectral data, we demonstrate that the fluorescence hyperspectral imaging system can identify different kinds of oil and recognize the oil film thickness. The fluorescence hyperspectral imaging system can be used in oil spill detection, resource exploration, natural disaster monitoring, environmental pollution assessment, and many other fields.

https://doi.org/10.1364/AO.432851

1. INTRODUCTION

Marine oil pollution is a serious "disease" for the world, which not only breaks the growth and reproduction environment of marine animals and plants but also threatens human healthy [1]. If the oil pollution can be monitored in time, it will be of great significance not only for the guidance of the cleanup work but also for the protection of the marine environment. At present, among the numerous sensors used in marine oil pollution monitoring, laser-induced fluorescence (LIF) [2–4] is the most effective oil detection technology. It uses the phenomenon in which the polycyclic aromatic hydrocarbons (PAHs) and their compounds contained in oil can generate excited electrons after absorbing UV excited light to realize the accurate identification and detection of oil target and oil film thickness. However, the laser radar is limited to a single band, and it cannot image the spatial-temporal distribution of oil targets. Hyperspectral imaging technology can obtain information of hundreds of continuous bands such as ultraviolet, visible, near-infrared, and infrared in the same spatial position, in addition to depicting fine spectral features such as the color and texture of the target. [5] Some researchers use one channel of the binocular camera as the spectral imaging channel and another channel as the spatial imaging channel, which can obtain the spectral image while obtaining the spatial image through the push-broom method. Based on the binocular vision method, the spatial depth information of the detection target can be obtained. They add depth information detection capability to the traditional hyperspectral technology. The system can obtain the spectral information of the target in the range of 400–700 nm, the obtained spatial image is clear, and the depth detection error is within 1%. However, handheld scanning was used to obtain the information, which can result in the distortion of the obtained spatial information, and which needs to be corrected by algorithm [6]. In 2006, French scientists used a FLS series laser combined with hyperspectral detector CASI-2 and GPS data to obtain a water body distribution map and oil spill distribution map with spatial resolution higher than 1 m [7]. In 2018, Zhejiang University developed a fluorescent hyperspectral imaging system using a *cemented doublet* and a CMOS detector with 1936 × 1216 pixels, and they tested typical oil samples by principal component analysis (PCA) and K-means clustering method [4]. In 2020, they also developed the Scheimpflug lidar system to monitor marine environment [8].

In this paper, a compact fluorescence hyperspectral imaging system based on a prism-grating-prism (PGP) structure was developed by using a 447 nm high-stability blue-violet diode

laser [9,10]. The system detector was a CMOS planar array detector of Basler's acA2040-90umNIR (2048 × 2048 pixels, pixel size is 5.5 μm). The system imaging spectrometer uses six lenses for imaging and collimation (the telecentric condition on both the objective and image sides can be realized). The spectral resolution is 2.5 nm, and the spectral range is 400–1000 nm. Three-dimensional cubic data of different oil films (two-dimensional spatial images and one-dimensional hyperspectral data) were collected by the system. We used the least noise separation algorithm for data dimension reduction and noise reduction processing, and we established a false color image to visualize the gradient area, uniform area, and nonuniform area of oil film thickness and the type of oil. We used a machine learning-support vector machine algorithm to achieve oil classification. The overall classification accuracy of different oil films is not less than 97%, and the kappa coefficient is not less than 0.94. It is of great significance to detect oil spill thickness, identify oil spill type, and monitor the marine environment.

2. FLUORESCENT HYPERSPECTRAL IMAGING SYSTEM

A. Design Principle of the Fluorescent Hyperspectral Imaging System

The fluorescence hyperspectral imaging system combines spectral detection techniques and imaging techniques. The imaging spectrometer can obtain the two-dimensional spatial information of the target by the push-broom method and can also obtain the corresponding one-dimensional hyperspectral information to form the three-dimensional data cube of the target. It is an important carrier for the traditional spectral analysis technology (qualitative and quantitative analysis) transformed into modern spectral analysis technology (qualitative, quantitative, timing, and positioning analysis).

Imaging spectrometers based on prism or diffraction grating have high spectral resolution and light energy utilization, but they are typical off-axis optical systems; their incident light beam and emergent light beam are not on the same axis, and they have problems such as large volume, complex structure, difficult assembly and debugging, and poor stability; and their fabrications of convex and concave gratings are difficult and costly. Aikio [11,12] first proposed an imaging spectrometer based on PGP in 1991, which was used in an aerial push-sweep spectral imager (AISA) to carry out aerial remote sensing experiments in 1993. The PGP imaging spectrometer is a straight cylinder type; its structure is simple, compact, and high integration, which has great application potential.

The PGP element is the core component of the PGP hyperspectral imaging system. Its volume phase holographic Bragg diffraction grating (VPH) has high light efficiency, which is very important for an imaging spectrometer, and its surface is smooth and easy to bond with the prism. Figure 1 is a schematic diagram of the optical principle of the PGP imaging spectrometer. The front-placed telescopic objective images the target at the slit and then collimator incident to the first prism of the PGP element by the collimator objective. Different wavelengths incident on the volume phase holographic grating at different angles and pass through the second prism after splitting through the grating, and then the central wavelength of the first-order diffraction

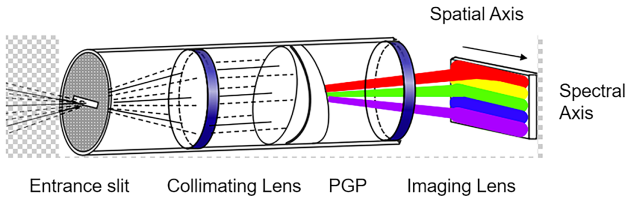

Fig. 1. Working principle of PGP structure imaging spectrometer.

Table 1. Technical Specifications of the Small Imaging Spectrometer

Specification		Value
Imaging	spectral region/nm	400–1000
	spectral resolution/nm	2.5
Spectrometer	size/mm	280 × 40 × 40
	Weight/kg	1.7
Front-placed lens	Focal length/mm	22
	F#	2.5
	FOV/(°)	26°
Imaging lens	Focal length/mm	40
	NA	0.2
Detector	Pixel size/μm	5.5 × 5.5
	Detector array size/pixed	2048 × 2048

is reflected back to the optical axis and then realizes the optical path coaxial structure. Finally, the scene is imaged through an imaging objective in the focal plane of the detector. This tubular direct vision (coaxial) structure enables the system to have low geometric aberration in both spatial and spectral directions, further guaranteeing optical performance.

B. Design of the Fluorescent Hyperspectral Imaging System

1. *Main Technical Indices of the Hyperspectral Imaging System*

According to the actual needs of remote sensing detection of oil spills, and considering the specific application background and system performance comprehensively, the design indices of the small imaging spectrometer are shown in Table 1.

2. *Design of the Front-Placed Telescopic System*

Compared with the visible light objective, the front lens of the refraction imaging spectrometer is special in its wider transmittance spectrum segment and its larger chromatic aberration, which is the difficulty of the design. The front telescopic objective system is designed by selecting the angle magnification and allocating the optical focus, and then calculating the relative aperture. The design result is shown in Fig. 2.

The performance of the telescopic system is shown in Fig. 3. The imaging effect was optimized by the ZEMAX optical design

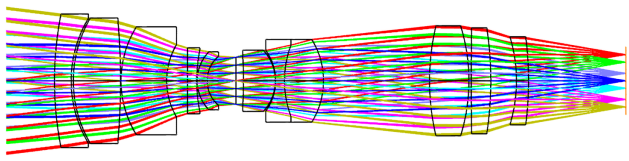

Fig. 2. Schematic diagram of the optical structure of the telescope.

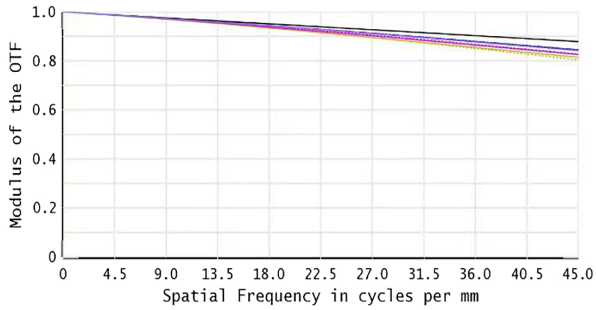

(a)

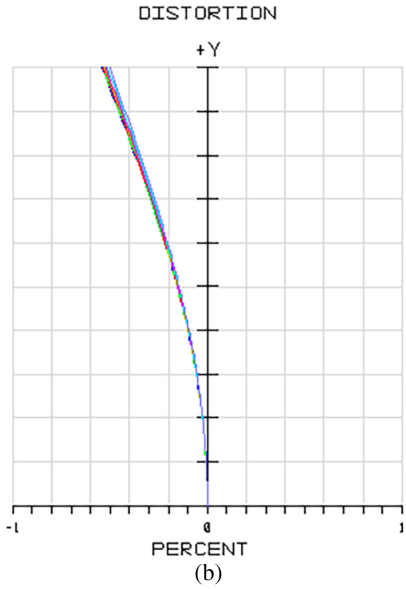

(b)

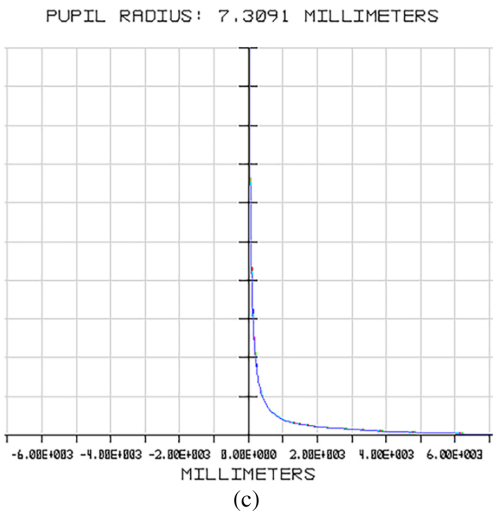

(c)

Fig. 3. Design results of the telescope. (a) MTF curve of the telescope, (b) spherical aberration curve of the telescope, and (c) chromatic aberration curve of the telescope.

software. From Figs. 3(b) and 3(c), it can be seen that the chromatic and spherical aberration of the system was well corrected, and the distortion and astigmatism were effectively controlled. The modulation transfer curve was shown in Fig. 3(a), and it can be seen that modulation transfer function (MTF) curve is greater than 0.8 at characteristic frequency 45lp/mm, which meets the imaging quality requirements of the front-facing telescope.

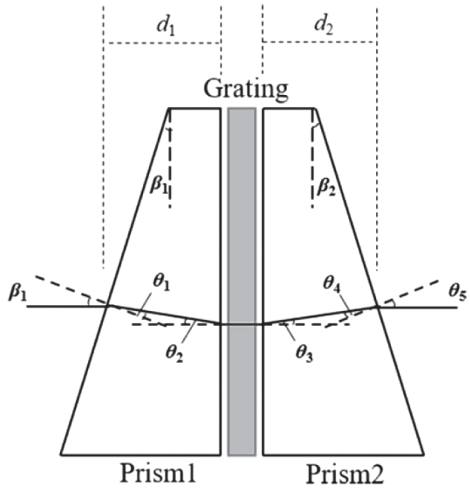

Fig. 4. PGP splitting element structure.

3. Design of the PGP Spectrometer

The PGP component (Fig. 4) is the main design content of the PGP spectroscopic system. The initial structure of the spectroscopic system is designed by solving the grating equation, the prism refraction law, and the Bragg constraint condition of the grating. The core of the PGP system is dispersion elements, which mainly considers the parameters including the material, the inclination angle of the prism, and the period of the grating. The two prisms' top angles $\boldsymbol{\beta}1$ and $\boldsymbol{\beta}2$ are important parameters to meet the requirements of direct radiation of the component [13].

In order to make the light still emergent along the optical axis, the condition between the inclination angle of the prism and the light emergence angle should be satisfied:

$$\boldsymbol{\theta}_5 = \boldsymbol{\beta}_2. \tag{1}$$

According to the law of refraction, the incident angle and the exit angle on the inclined surface of the prism are satisfied:

$$\mathbf{sin}\boldsymbol{\beta}_1 = \boldsymbol{n}\mathbf{sin}\boldsymbol{\theta}_1, \tag{2}$$

$$\boldsymbol{n}\mathbf{sin}\boldsymbol{\theta}_4 = \mathbf{sin}\boldsymbol{\theta}_5. \tag{3}$$

According to triangular geometry,

$$\mathbf{sin} = \boldsymbol{n}_{\boldsymbol{\lambda}}\mathbf{sin}(\boldsymbol{\beta}_1 - \boldsymbol{\theta}_2), \tag{4}$$

where $\mathbf{n}_{\boldsymbol{\lambda}}$ is the corresponding refractive index of prismatic glass at different wavelengths $\boldsymbol{\lambda}$. The volume holographic phase grating is a non-tilted transmission grating. The propagation vector of the grating is parallel to the surface, and there is a Bragg diffraction angle; when the incident angle is equal to the diffraction angle, the diffraction efficiency reaches the maximum, and the Bragg diffraction condition is satisfied:

$$\boldsymbol{\theta}_2 = \boldsymbol{\theta}_3 = \mathbf{arcsin}(\boldsymbol{\lambda}_C/2\boldsymbol{nd}), \tag{5}$$

Table 2. PGP Component Parameters

Parameter	Value
Number of grating lines/(lp/mm)	360
Thickness of sinking bottom/mm	3
Prism material	K9
Prism thickness/mm	5
Vertex angle of prism/(°)	13.95
Half height of PGP element/mm	15

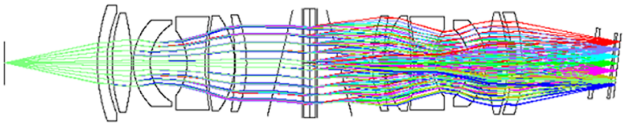

Fig. 5. Schematic diagram of the optical structure of the spectral imaging system.

where λ_C is the central wavelength, d is the grating constant, and then the tilt angle of the prism β_1 can be obtained as

$$\beta_1 = \arcsin[n\sin(\beta_1 - \arcsin(\lambda_C/2nd)]. \quad (6)$$

The exit angle β_λ corresponding to the non-central wavelength λ is

$$\beta_\lambda = \arctan[n_\lambda \sin\varphi/(n_\lambda \cos\varphi - 1)]. \quad (7)$$

The design parameters of the grating and prism are determined according to the overall index of the system, and the main technical indices of PGP are shown in Table 2. The two prisms are designed symmetrically with the same materials and parameters. The width of the prisms and d_2 have no direct relationship with the direct vision of light. In consideration of the purpose of reducing weight and easy processing, an appropriate value can be taken [14,15].

The collimation objective and imaging objective of the PGP splitting component adopt a symmetrical design, and the collimation mirror is the inverted form of the imaging mirror with exactly the same structural parameters, which simplifies the design difficulty and reduces the processing cost. The whole spectrum system's image side and object side are both telecentric light paths, which can effectively eliminate the vignetting phenomenon at the edge of the field and obtain uniform energy distribution on the image surface. The object side telecentric light path makes the PGP spectroscopic system more easily connected with the front telescopic system. We can deduce the focal length of the imaging objective lens according to the spectral range of the upper and lower emergence angle, when the spectral plane width is fixed. In the actual design process, the effective aperture of volume phase holography (VPH) grating should be considered. The parameters of the PGP element and the initial structural parameters of the imaging mirror should be input into ZEMAX software, and the design optimization should be carried out according to the design requirements. The optimized PGP spectrometer is shown in Fig. 5. The corresponding MTF curves of the full field of view and the full spectrum are shown in Fig. 6. The MTF is above 0.65 in Nyquist space frequency, and the design results meet the technical requirements.

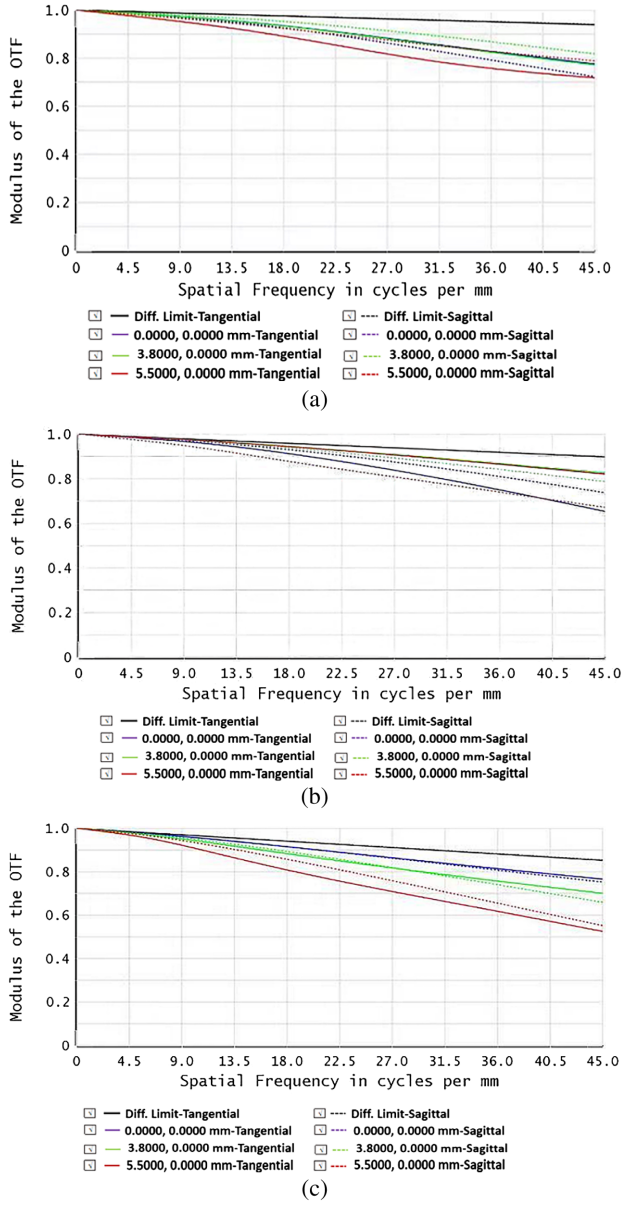

Fig. 6. MTF curve of the spectral imaging system: (a) 400 nm; (b) 700 nm; (c) 1000 nm.

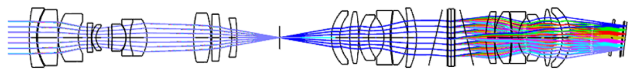

Fig. 7. Diagram of integrated optical structure.

4. Integrated Design and Prototype Development

After the optimized design of the telescopic objective and spectral imager was completed, integrating the front objective, the PGP splitting element, and the imaging objective together, and adding the incident slit, it can form a complete imaging spectrometer to further optimize the optical performance of the entire imaging spectrometer. The complete imaging spectrometer is shown in Fig. 7.

According to the result of the design and engineering implementation method, we developed the prototype as shown

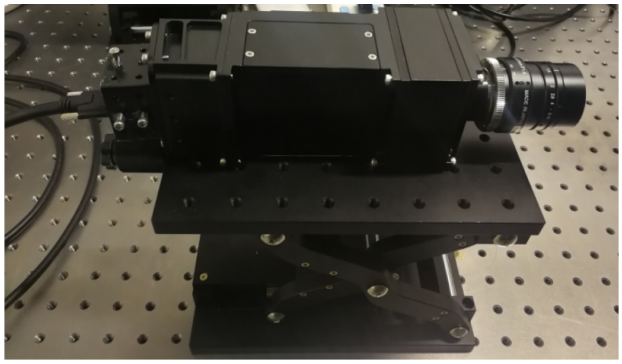

Fig. 8. Prototype of hyperspectral imager.

in Fig. 8. The lens materials of the telescope lenses, collimating lenses, and focusing lenses all come from GDGM GLASS (Chengdu, China). The types of glass include H-FK61, H-QK1, H-K1, H-ZF52, H-ZF4A, and so on. Antireflective coatings are used on all the lenses, and the optical transmittance of the lenses after coating is greater than 0.998. In the process of assembly and adjustment, the intermediate PGP spectral device is used as the assembly and adjustment reference so that the beam of intermediate wavelength within the spectral range can be parallel to the optical axis. Then the tilt and focus of the image plane are used as the compensation parameters, and the final assembly and adjustment can be completed.

The large diameter integrating sphere was used to carry out absolute radiation calibration. A mercury lamp and monochromator were used to calibrate the dispersion of the system. The spectroscopic image of the mercury lamp calibration is shown in Fig. 9(a). The radiation calibration image is shown in Fig. 9(b). The spectral resolution of the prototype was actually measured by He–Ne laser, and the performance test results were shown in Fig. 9(c). According to the radiation calibration results, the spectral calibration and fitting results are shown in Fig. 9(d), and the inhomogeneity of the detector response can be eliminated.

3. IMAGING EXPERIMENT OF SPECTRAL IMAGING SYSTEM

A. Process of Fluorescence Hyperspectral Imaging

The experiment site of the oil spill detection experiment was carried out in a darkroom; the experimental device for oil spill detection is shown in Fig. 10(a), and the experiment of excitation fluorescence by laser irradiation on an oil sample pool is shown in Fig. 10(b).The laser transmitting system includes the laser whose wavelength is 447 nm, cylindrical lenses, and reflectors. The laser was placed horizontally, cylindrical lenses were used to implement line laser scanning, and reflectors were used to implement the receiving and receiving signal at a common optical path. The receiving system is composed of a laser source filter, a PGP imaging spectrometer, and a computer. The PGP imaging spectrometer is placed on a 1 m high shelf, and the filter plate is installed in front of the lens through the bracket. The receiving system is aimed at the vessel containing the experimental oil sample, and the vessel was placed on the platform. The laser beam becomes linear after passing through the cylindrical mirror. By adjusting the reflective mirror, the

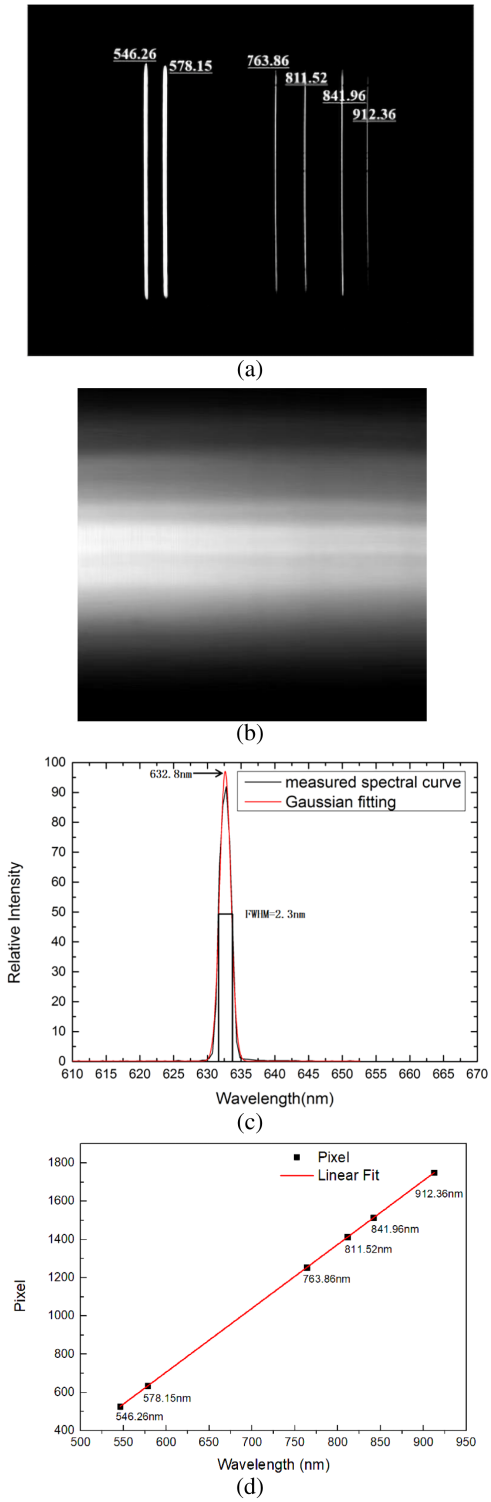

Fig. 9. Spectral image of laboratory calibration. (a) Spectroscopic image of mercury lamp calibration, (b) radiation calibration image, (c) He–Ne laser spectrum, and (d) spectral calibration and fitting results.

linear laser is incident onto the oil sample plate vertically. The laser excites fluorescence from the oil film, the fluorescence signal was received by PGP imaging spectrometer, and the collection of high fluorescence spectra of oil samples is realized by the push-broom method. The CCD camera receives the

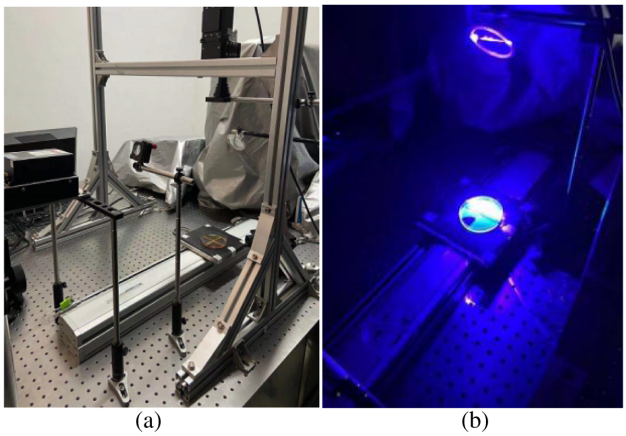

(a) (b)

Fig. 10. Experimental device environment: (a) the experimental device for oil spill detection; (b) the laser transmitting system.

Fig. 11. Fluorescence line image of turbine oil.

signal and converts it into digital signal before passing it to the computer software. Before collecting the data, we opened the software to debug the camera, including realizing that the image plane falls in the slit of the spectrometer and choosing the appropriate exposure time for the camera to ensure effective imaging. After debugging, the displacement table is used for the push-broom method, and the data are recorded. An original picture of fluorescence during the scanning process is shown in Fig. 11, which would later be combined with the rest of the picture in this scanning to form a complete data cube.

B. Oil Samples Preparations and Spectral Data Collection

Seawater, diesel, turbine oil, diesel oil, a four-grid sample dish, and normal sample dish were selected as experimental samples. The sample dish was placed on the workbench, and the oil sample was dripped into the prepared sample plate containing seawater through a burette to form a certain thickness of oil film to simulate oil spill in the sea. The four-grid oil sample and the turbine oil mixed seawater sample are shown in Fig. 12. The oil

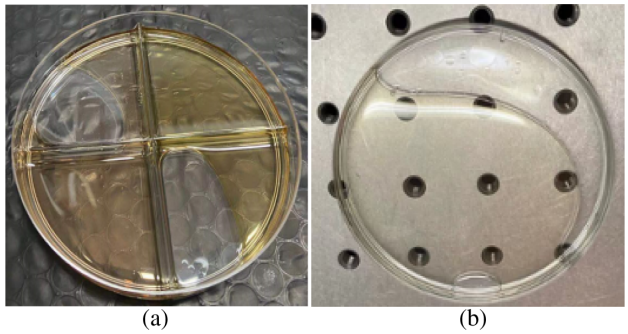

(a) (b)

Fig. 12. Oil samples: (a) four-grid oil sample; (b) turbine oil sample.

Table 3. Oil Sample Placement of Sample Dishes and Four-Grid Sample Dishes

Dish Number	First	Second	Third	
Oil Type	Diesel oil mixed seawater	Turbine oil mixed seawater	Wood oil mixed seawater	
Four-Grid Dish Number	First Area	Second Area	Third Area	Fourth Area
Oil Type	Turbine oil	Turbine oil mixed seawater	Wood oil	Wood oil mixed seawater

sample type placement of each sample dish is shown in Table 3. The displacement platform moved 5 mm per second. Every 30 ms, we took a fluorescent image. A total of 500 pictures was taken of each oil type.

C. Data Analysis

Due to the difference of time and conditions, the radiant energy value of fluorescence spectrum data is different. In order to effectively eliminate the deviation of spectral values caused by the difference of radiation energy, and moreover, to increase the uniformity of spectral morphology of similar substances and the difference of spectral morphology of different substances, in this study, several methods were performed. First, the spectral data of the oil sample was normalized, and the spectral data of the selected oil sample region was averaged and Savitzky–Golay smoothed [16]. Second, the minimum noise separation transformation (MNF) [17] was used to feature extraction and denoise. The MNF steps are as follows.

Assume that the original image size is $m \times f$, where m represents the total number of the band and f represents the total number of image pixels in a single band. The image vector Z_i of the ith band is composed of noise vector N_i and noiseless vector V_i, where $i = 1, 2, \ldots, m$:

$$\mathbf{Z_i} = \mathbf{N_i} + \mathbf{V_i}. \tag{8}$$

After filtering, the covariance matrix $\mathbf{C_Z}$ and $\mathbf{C_N}$ of the image vector $\mathbf{Z}$ and the noise vector $\mathbf{N}$ are obtained, and then the matrix diagonalization is made:

$$D_i = U_i^T (C_N{}^{-1} C_Z) U_i. \tag{9}$$

The eigenvalues of diagonalized matrices **D** are arranged from large to small. The eigenvectors have no correlation with each other, the signal-to-noise ratio is arranged from large to small, and the processed image vector is as shown as follows:

$$X_i = U_i^T Z_i. \tag{10}$$

The first component $\mathbf{X}_1$, second component $\mathbf{X}_2$, and third component $\mathbf{X}_3$ of the vectors are selected to build the false color composite image. **N** pixels of different oil sample areas were taken as the sample set of training data $\{\mathbf{x_j}, \mathbf{y_j}, \mathbf{j} = 1, 2, \ldots, \mathbf{N}, \mathbf{x} \in \mathbf{R^D y} \in \{1, 2, 3\}\}$ is the category label. A supervised learning algorithm-support vector machine (SVM) [18–20] was used to distinguish different types of oil samples. The SVM steps are as follows.

Assume the average vector $\mathbf{x_j}$ of all vectors in the oil species sample set is $\mathbf{x}'$, and then the Euld distance from the vector to the average vector $\mathbf{X}'$ is

$$S_j = \left|\left| x_j - x' \right|\right|. \tag{11}$$

Using the exponential Gaussian radial basis kernel function to transform the nonlinear problem into a linear problem in a high-dimensional space, the Gaussian radial basis kernel function is

$$k(x_j, x') = \exp\left(-\frac{\left|\left| x_j - x' \right|\right|^2}{2\delta^2}\right), \tag{12}$$

where $\delta^2 = \mathbf{0.333^2}$. Suppose high-dimensional classification discriminant function

$$\mathbf{g}(\mathbf{x}) = \mathbf{w} \cdot \mathbf{k}(\mathbf{x_j}, \mathbf{x}') + \mathbf{b}. \tag{13}$$

Then the classification surface equation is

$$w \cdot k(x_j, x') + b = 0. \tag{14}$$

We normalized the discriminant function and made the sample of the classification discriminant function $|\mathbf{g}(\mathbf{x})| = 1$. We can established the loss function

$$1/2 * ||w||^2. \tag{15}$$

The constraint condition is

$$y_j(w \cdot k(x_j, x') + b) \geq 1. \tag{16}$$

Therefore, the Lagrange function can be defined as

$$\mathbf{L(w, b, a)} = \mathbf{1/2} * ||\mathbf{w}||^2 - \sum_{\mathbf{j}=1}^{\mathbf{N}} \mathbf{a_j}[\mathbf{y_j}(\mathbf{w} \cdot \mathbf{k}(\mathbf{x_j}, \mathbf{x}') + \mathbf{b}) - 1]. \tag{17}$$

$\mathbf{a_j} > 0$, the minimum value of the Lagrange function, is solved for **w** and **b**. If the Lagrange coefficient $\mathbf{a_i}^*$ is the optimal solution, then the weight coefficient of the optimal classification surface is obtained:

$$w^* = \sum_{i=1}^{N} a_j{}^* y_j k(x_j, x'). \tag{18}$$

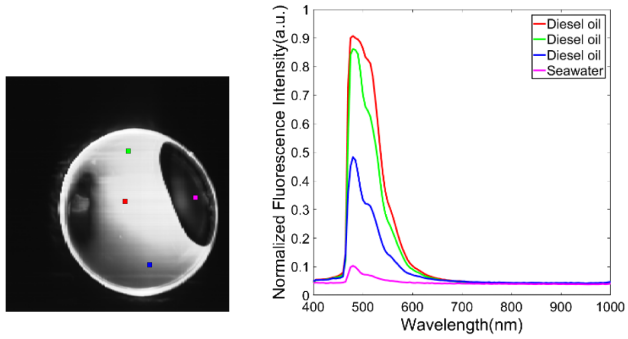

(a) (b)

Fig. 13. Diesel oil sample's fluorescence spectrum detection results: (a) fluorescence hyperspectral monochromatic image (480 nm) of the diesel oil sample; (b) fluorescence spectrum curve of different areas of the diesel oil sample.

Solve any non-zero samples $\mathbf{a_j}^*$, determine the classification threshold point $\mathbf{b}^*$, and get the optimal classification function

$$f(x) = \mathbf{sgn}\left(\sum_{j=1}^{N} a_j{}^* y_j k(x_j, x') + b^*\right). \tag{19}$$

Then, output the type of the oil samples.

4. RESULTS AND DISCUSSION

A. Fluorescence Spectra

The fluorescence hyperspectral monochromatic images of all the bands were obtained by stitching and clipping the collected fluorescence line spectral images of each oil sample. The monochrome fluorescence hyperspectral images of a certain band of each oil sample are shown in Figs. 13(a)–16(a). The red, green, blue, and purple regions are selected from the monochrome images to calculate the fluorescence spectrum mean value and the Savitzky–Golay smooth of the region. After the above signal processing, the peak intensity of the fluorescence spectrum can be observed. The fluorescence spectrum curves corresponding to the above regions are shown in Figs. 14–16(b).

Figures 13(a)–15(a) are the fluorescent hyperspectral monochrome images of diesel oil, turbine oil, and wood oil in a certain band, respectively. The red, green, blue, and violet curves in Figs. 13(b)–15(b) correspond to the fluorescent hyperspectral curves of the red, green, blue, and violet regions of the image, respectively, in which the red, green, and blue regions are the oil film region, and the purple region is the seawater region. Figure 16(a) shows the fluorescent hyperspectral monochrome image of the oil samples in four-grid vessels. The red, green, blue, and violet curves in Fig. 16(b) correspond to the fluorescent hyperspectral curves of the red, green, blue, and violet regions in the monochrome image, respectively, in which the red and green regions are the turbine oil regions, and the blue and purple regions are the wood oil regions. It can be seen that the spectra of the oil film regions are different from those of the seawater region. As shown in Figs. 13–15, the purple region has no spectral peak in the seawater region, while the red, green, and blue regions have spectral peaks in the oil film region.

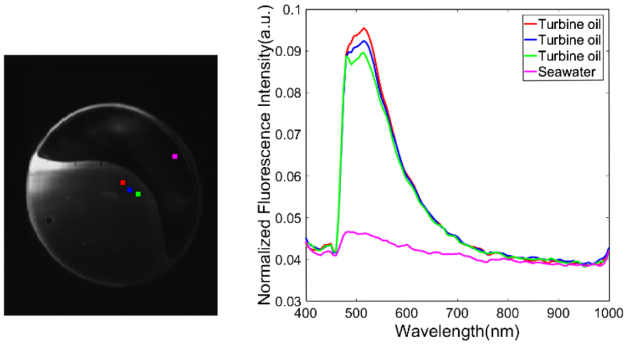

Fig. 14. Turbine oil sample's fluorescence spectrum detection results: (a) fluorescence hyperspectral monochromatic image (500 nm) of the turbine oil sample; (b) fluorescence spectrum curve of different areas of the turbine oil sample.

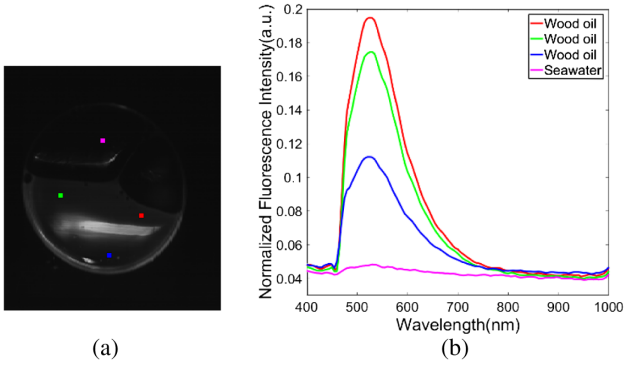

Fig. 15. Wood oil sample's fluorescence spectrum detection results: (a) fluorescence hyperspectral monochromatic image (470 nm) of the wood oil sample; (b) local fluorescence spectrum curve of different areas of the wood oil sample.

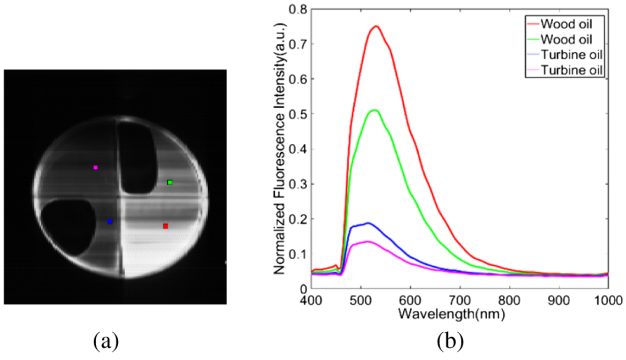

Fig. 16. Four-grid oil samples' fluorescence spectrum detection results: (a) fluorescence hyperspectral monochromatic image (500 nm) of the four-grid oil samples; (b) local fluorescence spectrum curve of different areas of the four-grid oil samples.

The shapes of the fluorescence spectrum lines of the same oil sample are the same, and the positions of fluorescence excitation peaks and the coverage range of fluorescence spectrum of different oil samples are different, which provides reliable information to guarantee for the qualitative analysis of oil sample composition, the acquisition of oil distribution in the target area, and the identification of oil types. The different regions of the same oil sample have different fluorescence spectra due to different oil film thicknesses, which provides a basis for further regional oil film thickness assessment.

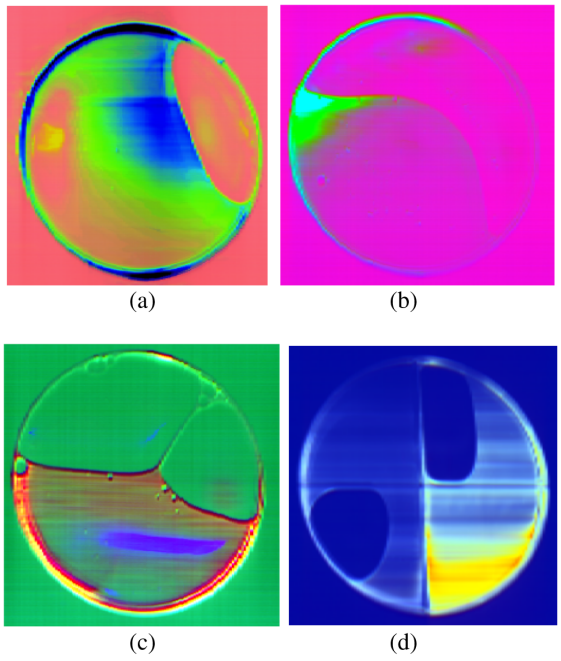

Fig. 17. Visual distribution image of (a)–(d). (a) Visual distribution image of diesel oil; (b) visual distribution image of turbine oil; (c) visual distribution image of wood oil; and (d) visual distribution image of four-grid oil.

B. Oil Classification and Distribution Analysis

In order to assist the identification of oil spill type and oil spill thickness, the oil film situation is visualized on the whole. The spectral data of oil samples are normalized, and MNF is used to select the first component, the second component, and the third component to establish the false color composite image. Figures 17(a)–17(c). show the visualized oil thickness information image of diesel oil, turbine oil, and wood oil, and Fig. 17(d) shows the visualized oil thickness information and oil type information images of four-grid oil samples.

Figures 17(a)–17(c) show that the fluorescence intensity in some areas is consistent, while the fluorescence intensity in some areas is obviously different, and the fluorescence intensity in other areas is gradually changed. It can be seen that the oil film thickness distribution is uneven, and the boundary between the oil film and the seawater area is obvious. As shown in Fig. 17(d), the color of the wood oil area on the left of the vessel is not significantly changed, and the relative fluorescence intensity is weak, while the color of the turbine oil area on the right of the vessel is significantly changed, and the relative fluorescence intensity is strong. It can be seen that under the same test conditions, the fluorescence excitation efficiency of different oil samples is different. Compared with a laser imaging system, the fluorescent hyperspectral imaging system not only obtains spectral information but also obtains the space image information. By establishing the color image, the oil film image can be

visualized. The areas with gradual change of oil film thickness, the areas with uniform distribution of oil film thicknessor non-uniform distribution of oil film thickness, and oil species can be visually seen through the images. It provides a useful visual reference for the system to detect oil spill thickness and identify oil species.

C. Oil Thickness Estimation

Hoge and others [21,22] used LIF detection technology to evaluate oil film thickness by using an inversion algorithm, and they concluded that if the laser light intensity reflected from the oil spill surface is less than the saturated fluorescence intensity of the oil spill, the received fluorescence signal intensity changes with the change of the oil film thickness. Therefore, in order to qualitatively monitor the relationship between the fluorescence intensity of the oil and its thickness, in our experiment, we choose diesel as the sample oil and used point laser or line laser for the fixed point measurement in our experiment. The thickness range was selected from 300 to 1050 um at 150 μm intervals. We added diesel oil to the surface of seawater in a container whose diameter is 2.9 cm. The volume of diesel oil is accurately measured by a syringe. According to the volume, the thickness of diesel oil can be estimated. Then, we captured 10 fluorescence images at time intervals of 1s at a particular diesel oil area for every oil thickness, and we took the average fluorescence intensity as the fluorescence intensity of the oil film thickness. Figure 18(a) shows the mean fluorescence spectra of oil films of different thickness. Figure 18(b) shows the linear regression analysis results of fluorescence intensity at 500 nm and diesel film thickness, and the determination coefficient $R2 = 0.9920$ was obtained. This experiment shows the feasibility of measuring oil thickness.

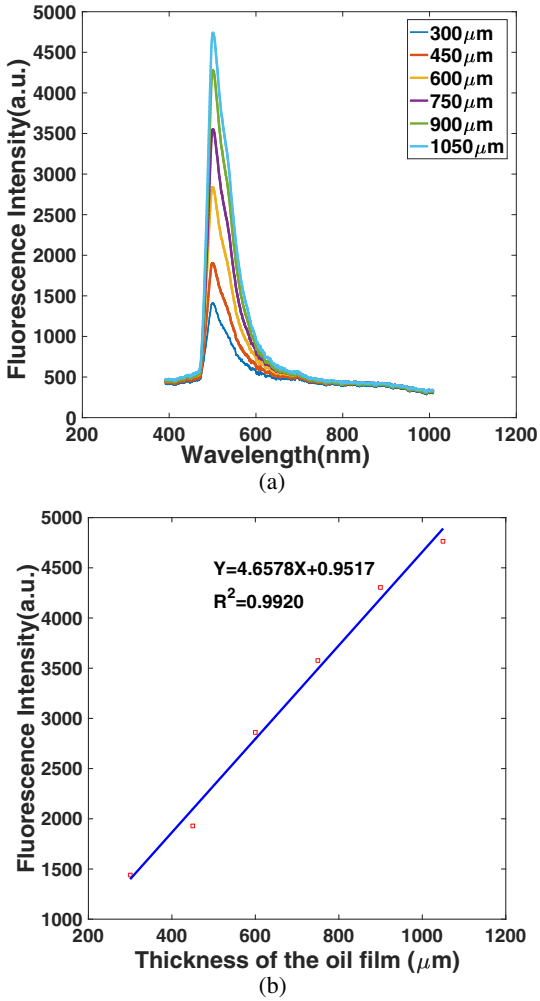

Fig. 18. Relationship between different oil film thickness and fluorescence intensity: (a) the fluorescence intensity of the different oil film thicknesses; (b) the fitted curve between the fluorescence intensity at the peaks (500 nm) with the different oil film thickness.

D. Classification Results and Evaluation

SVM is a classic supervised classification algorithm. In 2020, Jiao *et al.* [23] identified the origins and varieties of tetrastigma by using a dual-mode microscopic hyperspectral imager and the supervised classification algorithm SVM. In 2021, Xu *et al.* [24] classified, identified, and estimated the growth stage of microalgae by using a transmission hyperspectral microscopic imager (THMI) and SVM. In this paper, the collected fluorescence hyperspectral data of diesel oil, turbine oil, wood oil, and four-grid oil samples were reduced to MNF1, the first component of MNF, the second component of MNF2, and the third component of MNF3. Then, N pixels from different regions of the oil samples were selected as the training data of the SVM supervised classification algorithm. The separability of the training data [25] is larger than 1.5. The selections of the training data set are shown in Fig. 19. By using SVM processing, classification types and spatial distribution of diesel oil, turbine oil, wood oil, and four-grid oil samples are shown in Fig. 20.

In order to quantitatively measure the quality of the results of image classification, this paper evaluates the processing results through the overall classification accuracy T and kappa coefficient, where

$$\mathbf{T} = \sum_{\mathbf{i}=1}^{\mathbf{K}} \frac{\mathbf{M_{ii}}}{\mathbf{N}}, \tag{20}$$

$$\mathbf{Kappa} = \left(\mathbf{N}\sum_{\mathbf{i}}^{\mathbf{K}}\mathbf{M_{ii}} - \sum_{\mathbf{i}}^{\mathbf{K}}(\mathbf{M_i}\mathbf{M_{+i}})\right) \Big/ \left(\mathbf{N}^2 - \sum_{\mathbf{i}}^{\mathbf{K}}(\mathbf{M_i}\mathbf{M_{+i}})\right). \tag{21}$$

M is a confusion matrix of $\mathbf{K} \times \mathbf{K}$ obtained from the comparison between the image classification result graph and the real ground object, $\mathbf{K}$ is the number of oil product types, $\mathbf{M_{ij}}$ represents the number of samples in which type j is classified as type i. $\sum_{\mathbf{i}}^{\mathbf{K}}\mathbf{M_{ii}}$ represents the number of pixels classified, and $\sum_{\mathbf{i}}^{\mathbf{K}}(\mathbf{M_i}\mathbf{M_{+i}})$ represents the sum of the total number of pixels of all categories multiplied by the total number of pixels of the categories. The overall classification accuracy and kappa coefficient [26,27] of the classification results are shown in Table 4.

According to the evaluation of classification results, the overall classification accuracy of single diesel oil and single wood oil film is 100%, and the kappa coefficient is 1. The kappa coefficient of turbine oil is 0.9497, and the kappa coefficient of four-grid oil is 0.9525. Combining with the classification image in Fig. 20(b), there are scattered oil film signals in the seawater area where the turbine oil vessels are placed. It may be that there

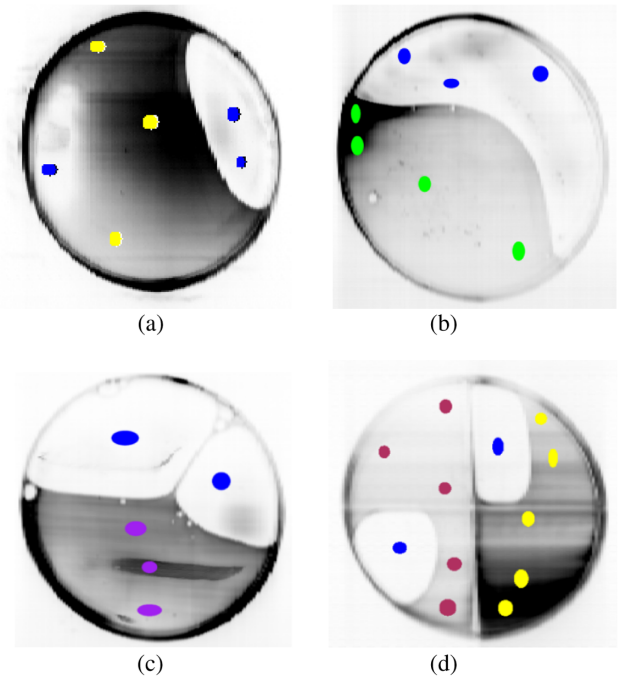

Fig. 19. Training data set area for SVM (a)–(d). (a) SVM training data set area of diesel oil; (b) SVM training data set area of turbine oil; (c) SVM training data set area of wood oil; (d) SVM training data set area of four-grid oil.

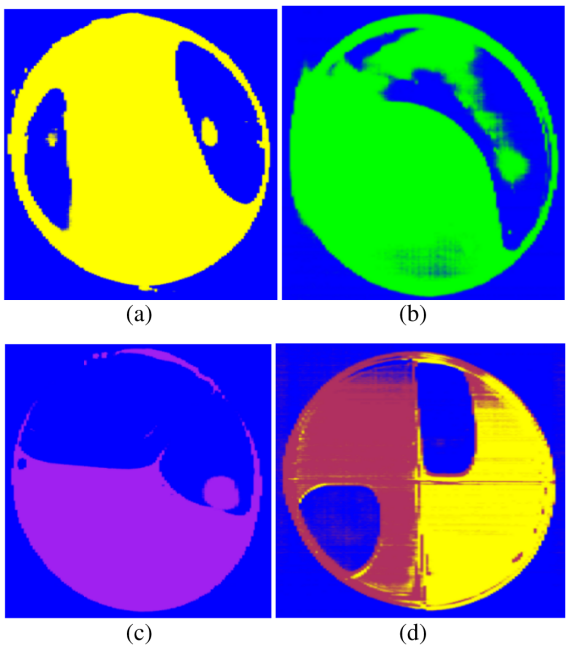

Fig. 20. SVM classification result of (a)–(d). (a) SVM classification result of diesel oil; (b) SVM classification result of turbine oil; (c) SVM classification result of wood oil; (d) SVM classification result of four-grid oil.

are non-seawater pixel elements in the seawater training data set selected, which are taken as turbine oil elements for analysis in SVM algorithm. On the other hand, the low fluorescence excitation efficiency of turbine oil may lead to weak fluorescence signal of steam engine oil. The intensity of fluorescence signal in some areas is even similar to that in the seawater area, which leads to the relatively low kappa coefficient. Combining with the visual image in Fig. 19(d), we find that the relative fluorescence intensity span of the wood oil film is obvious, while the relative fluorescence intensity span of the turbine oil is not obvious. The turbine oil region's and wood oil region's darkest colors are close to the color of the seawater, and the relative fluorescence intensity of the two oil films in our experiment is greatly different. The oil film regions with higher relative fluorescence intensity are easier to detect and distinguish, while the oil film regions with lower relative fluorescence intensity can be misjudged more easily. Therefore, the selection of training data sets in SVM and the combination of different oil films will affect the accuracy of system recognition.

Table 4. Overall Classification Accuracy and Kappa Coefficient of Diesel Oil, Turbine Oil, Wood Oil, and Four-grid Oil Samples

Oil Type Evaluation Index	Diesel Oil	Turbine Oil	Wood Oil	Four-Grid Oil
Overall classification accuracy	100.0%	97.57%	100.0%	97.53%
Kappa coefficient	1.000	0.9497	1.000	0.9602

5. CONCLUSIONS

A compact fluorescence hyperspectral imaging system based on a PGP structure is designed in this paper, and it is convenient for installation and adjustment and has a compact structure. The MTF curve of the telescopic system is greater than 0.8 at the characteristic frequency of 45 lp/mm, and the MTF curve corresponding to the full field of view and the full spectrum of the PGP spectrometer is greater than 0.65 at the Nyquist space frequency. After testing and calibration, the spectral resolution of the system is 2.5 nm, and the spectral range is 400–1000 nm. Three-dimensional data cubes (two-dimensional spatial images and one-dimensional hyperspectral data) of different oil samples were established through fluorescence hyperspectral imaging detection of different types of oil samples. MNF and SVM were used to process the data, and visual images of the thickness and spatial distribution of different oil samples were obtained. The overall classification accuracy was over 97%, and the kappa coefficient was above 0.94. It provides a technical foundation for qualitative analysis of marine oil spill composition, oil spill distribution in a target area, oil spill type identification, and oil film thickness assessment. The fluorescence hyperspectral imaging system developed in this paper is not only suitable for laboratory detection of different types of oil but also suitable for oil spill detection on ships and unmanned aerial vehicles at night or at other weak-background-light environment conditions. It provides a way of thinking for oil spill detection and has great significance for marine environmental protection.

Funding. National Key Research and Development Program of China (2018YFF01011003); Key Project of major subject of new and old kinetic energy conversion in Shandong Province (2020XJDN010039); National Natural Science Foundation of China (41575023, U2006209); Central University Basic Research Fund of China (202065004); Key Technology Research and Development Program of Shandong (2020CXGC010706);

Jilin Province Science and Technology Development Plan Project (20190302083GX); Key Deployment Project of the Marine Science Research Center of the Chinese Academy of Sciences (COMS2019J04); Consulting Research Project of Chinese Academy of Engineering (2020-XZ-5).

Disclosures. The authors declare no conflicts of interest.

Data Availability. Data underlying the results presented in this paper are not publicly available at this time but may be obtained from the authors upon reasonable request.

REFERENCES

1. S. Qayum and W. D. Zhu, "An overview of international and regional laws for the prevention of marine oil pollution and 'International obligation of Pakistan'," Int. J. Mol. Sci. **47**, 529–539 (2018).
2. J. Steffens, E. Landulfo, and L. C. Courrol, "Application of fluorescence to the study of crude petroleum," J. Fluoresc. **21**, 859–864 (2011).
3. E. Baszanowska and Z. Otremba, "Spectral signatures of fluorescence and light absorption to identify crude oils found in the marine environment," J. Eur. Opt. Soc. Rapid Publ. **9**, 14029 (2014).
4. W. T. Jiang, J. W. Li, and X. L. Yao, "Fluorescence hyperspectral imaging of oil samples and its quantitative applications in component analysis and thickness estimation," Sensors **18**, 4415 (2018).
5. M. F. S. Fouan and McKay, "Hyperspectral remote sensing: a new approach for oil spill detection and analysis," Ph.D. thesis (George Mason University, 2003).
6. F. H. Cai, T. C. Wang, and J. J. Wu, "Handheld four-dimensional optical sensor," Optik **203**, 164001 (2020).
7. M. Lennon, S. Babichenko, and N. Thomas, "Detection and mapping of oil slicks in the sea by combined use of hyperspectral imagery and laser induced fluorescence," Earsel Eproc. **5**, 120–128 (2006).
8. S. L. He, X. Chen, and S. Li, "Small scale hyperspectral spectrometer and LIDAR's applications in marine," Infrared Laser Eng. **49**, 2 (2020).
9. Q. S. Xue, B. Yang, and F. P. Wang, "Compact, UAV-mounted hyperspectral imaging system with automatic geometric distortion rectification," Opt. Express **29**, 6092–6112 (2021).
10. Q. S. Xue, Q. Sun, and F. P. Wang, "Underwater high-precision 3D reconstruction system based on rotating scanning," Sensors **21**, 1402 (2021).
11. B. Braam, J. Okkoen, and M. Aikio, "Design and first test results of the Finnish airborne imaging spectrometer for different applications (AISA)," Proc. SPIE **1937**, 142–151 (1993).
12. A. Mauri, "Hyperspectral prism-grating-prism imaging spectrograph," (Technical Research Centre of Finland, 2001).
13. S. B. Zhu, Y. Q. Ji, and G. B. Gong, "Design of prism-grating-prism spectral imaging system," Acta Photon. Sinica **38**, 2270–2273 (2009).
14. G. H. Xiao, R. Shu, and Y. Q. Xue, "Design of microscopic hyperspectral imaging system," Opt. Precis. Eng. **12**, 367–372 (2004).
15. S. B. Zhu, "Design of spectral imaging system based on PGP spectroscopic device," (Suzhou University, 2009), 20–22.
16. C. Ruffifin and R. L. King, "The analysis of hyperspectral data using Savitzky-Golay fifiltering-theoretical basis," in *International Geoscience and Remote Sensing Symposium (IGARSS)*, Hamburg, Germany, 28 June–2 July, 1999, Vol. **2**, pp. 756–758.
17. A. A. Green, A. Berman, and P. Switzer, "A transformation for ordering multispectral data in terms of image quality with implications for noise removal," IEEE Trans. Geosci. Remote Sens. **26**, 65–74 (1998).
18. C. Cortes and V. Vapnik, "Support vector networks," Machine Learn. **20**, 273–297 (1995).
19. O. Chapelle, P. Haffner, and V. N. Hapnik, "Support vector machine for histogram-based image classification," IEEE Trans. Neural Netw. **10**, 1055–1064 (1999).
20. C. Kotropoulos and I. Pitas, "Segmentation of ultrasonic images using support vector machines," Pattern Recogn. Lett. **24**, 715–727 (2003).
21. F. E. Hoge, "Oil film thickness using airborne laser induced oil fluorescence backscatter," Appl. Opt. **22**, 3316–3318 (1983).
22. Y. N. Chen, R. F. Yang, and N. J. Zhao, "Experimental study on quantitative detection of oil slick thickness based on laser-induced fluorescence," Spectrosc. Spectral Anal. **39**, 3646–3652 (2019).
23. C. W. Jiao, Z. P. Xu, and Q. W. Bian, "Machine learning classification of origins and varieties of Tetrastigma hemsleyanum using a dual-mode microscopic hyperspectral imager," Spectrochim. Acta A **261**, 120054 (2021).
24. Z. P. Xu, Y. M. Jiang, and J. L. Ji, "Classification, identification, and growth stage estimation of microalgae based on transmission hyperspectral microscopic imaging and machine learning," Opt. Express **28**, 30686–30700 (2020).
25. J. A. Richards, "Classifier performance and map accuracy," Remote Sens. Environ. **57**, 161–166 (1996).
26. J. Cohen, "A coefficient of agreement nominal scales," Educ. Psychol. Meas. **20**, 37–46 (1960).
27. R. G. Pontius, "Quantitive error versus location error in comparison of categorical maps," Photogramm. Eng. Remote Sens. **66**, 1011–1016 (2000).